Modeling and Simulation of Lipid Monolayers as Surfactant in Lung Alveoli

Annelene Wittenfeld, Andrey Ryskin, and Wolfgang Alt

1 Biological Function of Surfactant Lipids for the Breathing Cycle

The concave cellular surface inside lung alveoli is covered by a thin water film with surfactant on top, whose continued preservation is essential for the rapid oxygen and carbon dioxide exchange between air and lung tissue. Therefore, in order to guarantee film stability during the regular breathing cycle of inhalation (expansion of lung alveoli) and exhalation (their compression), the surfactant lipid-protein layer must possess strong adaptive properties. This becomes even more important in events of sudden expansion or compression of the lung, for example, while coughing. On one hand, the function of the surfactant layer is to strongly reduce surface tension for minimizing the work of breathing, which is achieved by forming highly ordered monolayers of amphiphilic lipid molecules. On the other hand, the layer has to be fluid enough to cover the expanding surface in a continuous and rapid fashion, which requires stochastic mobility of the lipid molecules.

Synthetic chemical models of efficient pulmonary surfactant, also used for medical treatment, contain specific mixtures of phospholipids (e.g. phosphatidylcholine, DPPC, palmitic acid, PA) and have been experimentally investigated under periodic compression-relaxation conditions [3]. A typical result can be seen in Fig. 1, which shows the quasistatic behavior as an isotherm plot (surface pressure versus inverse density). During the first two compression cycles the pressure-density curve shows an obvious hysteresis effect. The overall pressure decreases more rapidly at the beginning of the expansion periods (to the left), compared to a more steady increase during the compression periods (to the right). This is a strong indication

A. Wittenfeld (✉) · A. Ryskin · W. Alt
Abteilung Theoretische Biologie, Institut für Zelluläre und Molekulare Botanik, Rheinische Friedrich-Wilhelms-Universität Bonn, Kirschallee 1-3, D-53115 Bonn, Germany
e-mail: wolf.alt@uni-bonn.de; a.wittenfeld@gmx.de

M. Griebel (ed.), *Singular Phenomena and Scaling in Mathematical Models*,
DOI 10.1007/978-3-319-00786-1_8,

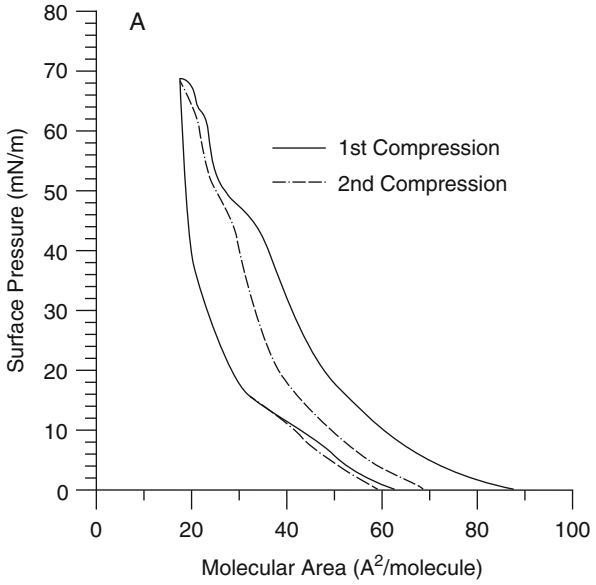

Fig. 1 Quasistatic isotherm plot of surface pressure versus area per lipid molecule (inverse density) for an artificial lipid mixture as a model of surfactant layer on lung alveoli. The two compression-expansion trajectories are cycling counter-clockwise. (From [3], Fig. 1A)

for transformation processes, such as association and dissociation, to occur in the different periods and phases.

Moreover, atomic force microscopy of such surfactant monolayers has revealed remarkable inhomogeneities in height and stiffness (see [1], Fig. 1). One observes larger and mostly rounded patches of thick homogeneous molecular layers, indicating regions of strongly ordered lipid molecules (liquid condensed phase) and, in-between, smaller and more fuzzy patches of thinner layers, indicating regions of non-ordered and diffusing lipid molecules (liquid expanded phase). The interface between these two kinds of patches appears to be quite sharp, suggesting a relatively fast transition zone between the ordered and disordered phase.

These spatial phase separation phenomena together with the observed hysteresis dynamics have important biophysical functions: regions of more fluid disordered monolayers serve as a mechanical buffer of more easily compressible lipid molecules; in addition, they serve as a chemical reservoir of diffusing lipids to be supplied for insertion into the ordered regions of the monolayer. However, in order to describe and understand the full dynamics of these biophysical/chemical processes, one needs detailed mathematical models and their subsequent numerical simulation on various spatio-temporal scales. For a 3-d molecular dynamics simulation see [4], for a general 3-d continuum fluid-diffusion simulation including thin film dynamics on a periodically extending alveolar surface see [5].

Here we present recent modeling and simulation results for two different scaling approaches, showing certain connections with each other. The first is a stochastic

multiparticle model of rod-like lipid molecules on a microscopic scale (space: $\sim$ 10–500 nm; time: $\sim$msec) with appropriate classical interaction potentials (Sect. 2). The second describes a deterministic continuum two-phase fluid model on a mesoscopic scale (space: $\gtrsim$ μm; time: $\gtrsim$ sec) with an appropriately chosen free energy function and flow properties (Sects. 3–5).

2 Microscale Stochastic Multi-particle Model

We study a system of N stiff rod-like particles of fixed length L, which are partially submersed in water at a sharp and flat water-air interface. In order to model the amphiphilic properties of lipids, these rods are assumed to have a hydrophilic head for length variable $0 < s < L/4$, and a hydrophobic tail for $L/4 < s < L$ (see Fig. 2). The rods interact by means of a continuous, distance-dependent force density $\mathbf{f}(s)\,ds$ on each rod, accounting for the amphiphilic properties of the rods as well as their location and motion with respect to the water-air interface. For simplicity, we restrict our simulation model to a two-dimensional spatial configuration, so that the rods are not allowed to overlap with each other.

We denote by $\delta = \delta(r, s)$ the distance of two points r, s on distinct rods $i \neq j$. The interactive force between head of rod i $(0 < r < L/4)$ and tail of rod j $(L/4 < s < L)$ is purely repulsive, inversely proportional to the distance δ with strength coefficient α. For head-head and tail-tail interaction we use a Lennard-Jones potential, valid for various kinds of particles and molecules,

$$V_{\varepsilon,\sigma}(\delta) = 4\varepsilon\left(\left(\frac{\sigma}{\delta}\right)^{12} - \left(\frac{\sigma}{\delta}\right)^{6}\right) \tag{1}$$

with different scaling coefficients $\varepsilon > 0$ and $\sigma > 0$.

Since the upper part of each rod is hydrophobic and the lower hydrophilic, there is a kind of capillary force pulling each subpart into its optimal medium by tending to reduce the length of the amphiphilic mismatch g, see Fig. 2.

Here we assume a simple proportionality

$$F_{\text{wat}} = k_s\, g, \tag{2}$$

with effective elasticity coefficient k_s. This water surface force acts onto the center of the amphiphilic mismatch region in the 'wrong' medium, pointing towards the 'right' medium in direction parallel to the rod. Since a rod has a 'hydrophilic' and a 'hydrophobic' part, we need to ensure that it does not flip over. Therefore, as angular momentum, we assume an analogous non-linear term, modeled as to be induced by the surface tension acting on both sides of the rod:

$$M_{\text{wat}} = -k_\theta \left(\tan\big(\theta - 0.5\pi\big) + \tan^3\big(\theta - 0.5\pi\big)\right). \tag{3}$$

This momentum tends to turn the rod into an upright position ($\theta = 0.5\pi$). The first summand acts as a linear spring in case of small angle differences.

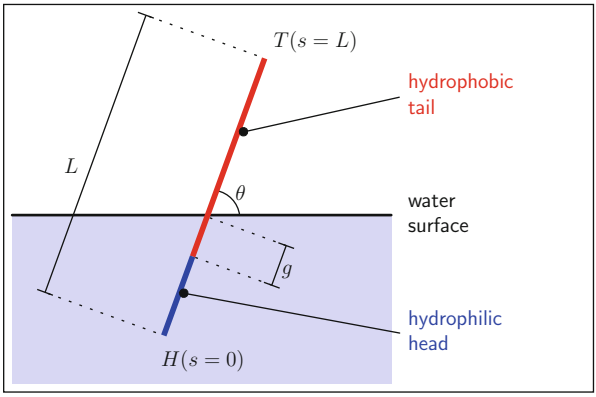

Fig. 2 Schematic picture of an amphiphilic rod and its location at a fixed water-air surface

The second summand represents a strong repulsive spring turning away from any parallel orientation with the water surface ($\theta = 0$ or π) in case of larger angle differences.

Additionally, we model local collision of rods with the surrounding smaller water and air molecules by means of a spatio-temporal stochastic Brownian sheet. On each segment of the discretized rod, we assume small and independent random forces, with amplitude adjusted via a parameter c_w representing the standard deviation of the corresponding Gaussian noise perpendicular to the rod. The perturbation along the rod is twice as large. Additionally, the process depends on the surrounding medium. If the segment of the rod is outside the water, the perturbation strength is one tenth as compared to a segment within the water. Accordingly, the stochastic force density is defined by

$$\mathrm{d}\,\mathbf{f}_{\text{brown}}(s,t) = \mathbb{D}(s)\,\mathrm{d}\mathbf{B}_{s,t} \tag{4}$$

with a corresponding amplitude matrix $\mathbb{D}(s)$. Finally, friction is considered to be proportional to the local velocity of a point on the rod,

$$\mathbf{f}_{\text{friction}}(s) = -\mathbb{F}(s)\mathbf{v}(s). \tag{5}$$

In diagonal representation, i.e. when the coordinate system is aligned with the rod, the friction matrix reads $\mathbb{F} = \operatorname{diag}(\gamma_\parallel, \gamma_\perp)$. The imposed drag perpendicular to the rod $\propto \gamma_\perp$ is twice as large as compared to the friction along the rod $\propto \gamma_\parallel$. Additionally, there are different γ-values for each surrounding medium, namely γ^A in air and γ^L in liquid, since the viscosity of the fluid is larger than the viscosity of air.

In this model, we treat the rod-like particles as rigid bodies. From the local force densities above, we calculate the effective center-of-mass force and the torque acting on each rod. The resulting Newtonian equations of motion are employed in their over-damped limit with vanishing inertia.

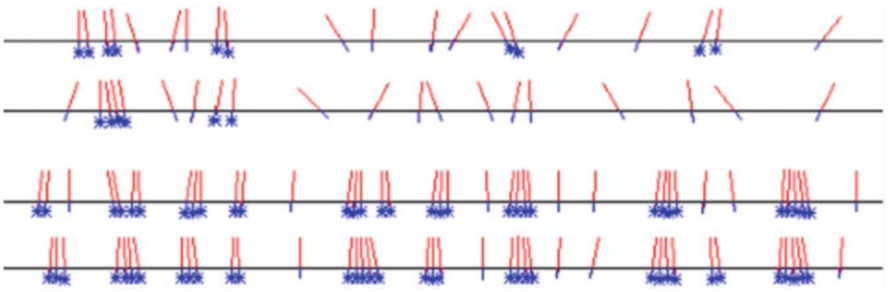

Fig. 3 Snapshots of simulation runs with N = 20 (*first* and *second row*) and N = 40 rods (*third* and *fourth row*), performed on a small interval of length $X = 900\,\text{nm}$, thus with densities $\rho = 0.022\,\text{nm}^{-1}$ and $\rho = 0.044\,\text{nm}^{-1}$, respectively. The *second* and the *fourth row* are about 300–400 ms later than the *first* and the *third*, respectively. Clustered rods are marked by a *star*

The simulation program is conceived in a highly optimized manner, including certain coding in assembler, on several cores at a time. The simulations are performed with different numbers N of rods with fixed length $L = 40$ (in an artificial length unit, comparable to nanometer, nm) initially distributed in random positions at the flat (periodic) waterline (of width $X = 22220\,\text{nm}$) and with randomly chosen angles, $0 < \theta_i < \pi$, but without intersections of the rods. Simulation runs are performed for 20,000,000 timesteps (in an artificial time unit, comparable to microseconds, μsec), thus for about 20 s, see Fig. 3 for typical lipid configurations appearing in two different simulations (with shorter width). After every 1,000 timesteps (thus each millisecond, msec) certain observables are extracted for data evaluation.

As a first evaluation, we quantify proximity of the simulated rods. Two rods i and j are defined to be clustered, if

$$|\theta_i - \theta_j| \le \beta_{\max} \quad \text{and} \quad |w_i - w_j| \le b_{\max}. \tag{6}$$

If a rod does not obey these relations with any other, it is said to be unclustered. Here, w_i denotes the horizontal position, at which the rod i crosses the waterline. The positive parameters $\beta_{\max}$ and $b_{\max}$ are suitably chosen thresholds, namely $\beta_{\max} = 10°$, $b_{\max} = 15$. As an observable we define the overall clustering

$$C = \frac{\text{number of clustered rods}}{\text{total number of rods } N} \tag{7}$$

of the simulated rods for every time step. Another observable is the polar order parameter

$$R = \frac{1}{N}\Big|\sum_i \widehat{e_i}\Big|, \tag{8}$$

where $\widehat{e_i} = (\cos\theta_i, \sin\theta_i)$ represents the unit vector along the i-th rod.

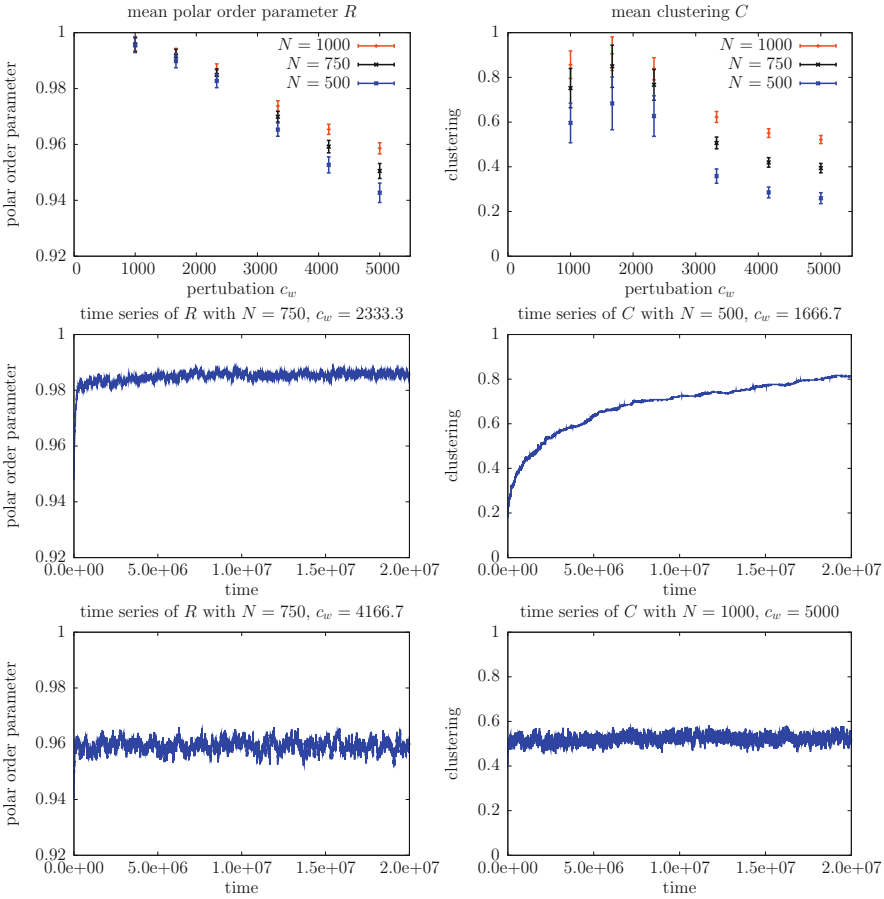

Fig. 4 In the plots above we show the mean polar order parameter R and clustering C depending on the perturbation c_w, for different particle numbers N. The plots below show examples of corresponding time series. Note that the essential parameters c_w and N vary, as separately indicated for each plot. The other simulation parameters are the same for all plots shown. The friction is $\gamma_{\parallel}^{L} = 300$, $\gamma_{\perp}^{L} = 600$ inside of the liquid and $\gamma_{\parallel}^{A} = 30$, $\gamma_{\perp}^{A} = 60$ outside. The remaining interactive force parameters are $\sigma_{tt} = 5$, $\varepsilon_{tt} = 100, \sigma_{hh} = 7.5$, $\varepsilon_{hh} = 20$, $\alpha = 1$ and $k_s = k_\theta = 25$

Time behavior of the observables (7) and (8) is presented in the lower part of Fig. 4 for a typical set of simulation parameters. For the polar order index R (plots in the left column), the overall behavior is almost the same for each simulation. Starting from a 'random' initial value $\sim$0.94, within less than 100 ms the index reaches a stationary value, about which it fluctuates, though with a slight adjusting increase in case of the smaller perturbation amplitude $c_w = 2333.3$. In contrast, the clustering index C (plots in the right column) shows a quite different behavior. For $c_w \leq 2333.3$ and every N, the index slowly approaches its potential stationary level

with an exponential rate of time scales more than 5 s. This also explains the large variances and the decreasing mean in the corresponding parameter plot (top right). For $c_w \geq 3300$, the stationary level of C is reached almost instantaneously, meaning that the 'clustering rate', i.e. the speed of cluster growth, is strongly dependent on the lipid mobility coefficient c_w. Further simulations could reveal a more detailed dependence.

The polar order index R exhibits a clear monotone dependence on c_w (top left plot in Fig. 4). Moreover, in the two parameter plots it can be seen that a higher density of rods leads to a higher value of both indices, clustering and polar order. The explanation for this feature is obvious: since the rods are generally closer at higher densities, their short-range interactions give rise to enhanced mutual alignment of adjacent rods. Thus, the rate of transition from 'disordered' rods (freely diffusing) to 'ordered' rods (mutually aligned in clusters) depends both on mobility and density of the modeled lipid molecules, amphiphilically embedded into the water surface.

3 Mesoscale Continuum Mixture Model

As shown by the stochastic microscopic model in the previous section, the temporal scale, on which clustering and order indices experience slow changes, lies in the range of 1–5 s. Also, sizes of ordered lipid clusters in this one-dimensional simulation model are in the range of 20–500 nm, which is up to ten times the rod length $L = 40\,\text{nm}$, whereas the mean distance of lipids in clusters is about 10 nm. Thus, when locally averaging the density of lipids, ρ, and the mean fraction of ordered lipids, φ, on the larger spatial scale $\gtrsim \mu\text{m}$, these quantities $\rho(t, x)$ and $\varphi(t, x)$ could be considered as continuously varying over the time scale of seconds.

Since the clusters of ordered lipids have quite sharp boundaries in the order of rod length $L = 40\,\text{nm}$, this spatial transition zone from the disordered to the ordered phase scales with a factor $\varepsilon \lessapprox 0.05$ compared to the μm length scale. Thus, the continuum phase field model defined and treated in [1], seems to be in accordance with the 'empirical' findings from the microscopic model, since the free energy of the continuous lipid monolayer system is defined by

$$f(\rho, \varphi) = f^0(\rho, \varphi) + \frac{\varepsilon^2}{2}|\nabla\varphi|^2. \tag{9}$$

Here $f^0(\rho, \varphi)$ is a suitable 'interpolation' between free energies in the single phases with densities $\rho_\alpha = \rho\,\theta_\alpha$ and volume fractions $\theta_1 = (1-\varphi), \theta_2 = \varphi$, for $0 \leq \varphi \leq 1$. They are chosen as canonical Gibbs energies

$$f_\alpha(\rho) = b_\alpha^0 \rho \left(\log(\rho/\rho_\alpha^0) - 1\right) + c_\alpha \tag{10}$$

with positive model parameters. The free energy f^0 can then generally (even for more than two phases) be written as

$$f^0(\rho,\theta) = \sum_\alpha \chi(\theta_\alpha)\left[f_\alpha(\rho) + b_\alpha^0 \rho\, \Lambda\left(\eta_\alpha(1-\theta_\alpha)\right)\right] \tag{11}$$

with an interpolating function $\chi : [0,1] \to [0,1]$ satisfying $\chi'(0) = \chi''(0) = 0$, $\chi'(1) = \chi''(1) = 0$, and with the monotone function $\Lambda(z) = z + (1-z)\log(1-z) : [0,1] \to [0,1]$ satisfying $\Lambda'(0) = 0$.

In addition to the χ-interpolation, for each phase α there appears an excess energy term $\eta_\alpha(\vartheta_\alpha)$ evaluated at the complementary volume fraction $\vartheta_\alpha = (1-\theta_\alpha)$. Here $\eta_\alpha(\vartheta_\alpha)$ represents an increasing 'reaction' function with $\eta_\alpha(0) = 0$, describing the amount of phase associations from other phases towards the α-component. The more 'other' molecules are locally available, the larger is the probability of transition to the α-component. Since 'binding sites' are limited as in usual chemical Michaelis-Menten kinetics, we suppose a corresponding transition kinetics of Monod type:

$$\eta_\alpha(\vartheta) = \frac{s_\alpha \vartheta}{1 + s_\alpha \vartheta/\kappa_\alpha}\,. \tag{12}$$

Here $s_\alpha > 0$ denote the transition strengths and $0 < \kappa_\alpha < 1$ the asymptotic saturation level, so that always $\eta_\alpha(\vartheta) < 1$. In the simulations below we choose $s_1 = 9$ and $s_2 = 4$, meaning that association to ordered lipids is about half as easy as their dissociation.

For a general thermodynamically correct theory of continuum mixture dynamics with corresponding equations for mass and force balances, we refer to the contribution by H.W. Alt and W. Alt in this volume [2]. For example, the total pressure $p^0 = \rho f'^0_\rho - f^0$ of the model above can be computed as

$$p^0(\rho,\theta) = \sum_\alpha \chi(\theta_\alpha)\ (1 + \eta_\alpha(1-\theta_\alpha))\ b_\alpha^0 \rho\,. \tag{13}$$

To characterize the special case of a two-phase ordered-disordered lipid monolayer system with total density $\rho(t,x)$ and volume fraction of ordered lipids $\varphi(t,x) := \theta_2(t,x)$, several particular assumptions have to be implemented.

- There is only one mean transport velocity for both phases, $\mathbf{V}$. We notice that according to the microscopic simulation model (in Sect. 2) all lipids are embedded into the water surface with part of their hydrophilic head region. Then the assumed mean velocity $\mathbf{V}$ can be interpreted as a bulk velocity of the lipid heads together with their surrounding water molecules near the surface. The differences $\mathbf{u}_\alpha = \mathbf{v}_\alpha - \mathbf{V}$ for the two phases are due to possible diffusive flow, which might be derived along the lines indicated in [2], Sects. 6–11.

This would be compatible with the following assumptions that have been made in [1]:

- In addition to transport velocity the mass balance equation for ρ contains a diffusive flux $-d_\varepsilon \nabla f'_\rho$ with inverse diffusion coefficient being interpolated as follows:

$$\frac{1}{d_\varepsilon} = \varphi \frac{1}{\varepsilon d_0} + (1-\varphi)\frac{1}{d_0}. \tag{14}$$

Here ε is the small positive constant defined above, meaning that the ordered lipids diffuse much less than the disordered ones.

- The surfactant monolayer as a fluid-like system on top of the water surface can be regarded as a viscous fluid, where the viscosity coefficients α, β are those of the water surface layer (α_0 and β_0) but increased by lipid shear forces. These are stronger for ordered lipids than for disordered ones. Therefore we define $\zeta = \{\alpha, \beta\}$ as $\zeta = \zeta_0 + (1-\varphi)\,\zeta_1 + \varphi\,\zeta_2$ with suitable positive constants.

Then two mass balance equations are complemented by one quasi-stationary force balance equation in the limit of low Reynolds number (high viscosity), namely

$$\partial_t \rho + \operatorname{div}(\rho \mathbf{V} - d_\varepsilon \nabla f'^0_\rho) = 0, \tag{15}$$

$$\partial_t \varphi + \mathbf{V}\nabla\varphi + f'^0_\varphi - \varepsilon^2 \Delta\varphi = 0, \tag{16}$$

$$\partial_j (p^0\,\delta_{ij} - \alpha(\partial_i V_j + \partial_j V_i) - \beta \partial_k V_k \delta_{ij}) = 0. \tag{17}$$

This is the (quasi-stationary version of the) system that has been investigated in [1]. In the following sections we report on some further results that have been obtained by modifying or extending the numerical methods used so far.

4 Sharp Phase Transition Approximation

In the limit of small $\varepsilon \to 0$ we obtain a fast transition layer of width ε, in which the phase transition equation (16) for φ and the mass conservation (15) for ρ in their quasi-steady-state limit for $\varepsilon = 0$ constitute a 3-dimensional ODE system of first order. For given 'density jump' levels $\rho_1 > 0$ and $\rho_2 > 0$ its solutions have to connect the two outer asymptotic states ($\varphi = 0, \rho = \rho_1$) and ($\varphi = 1, \rho = \rho_2$). Moreover, the ODE system contains a free parameter λ representing the difference between the interface velocity and the normal component of $\mathbf{V}$ at the interface. For more details see [1], Sects. 5 and 6.

The solution of this sharp transition problem is equivalent to finding a value λ such that a reduced 2-dimensional ODE system for the phase transition derivative $\psi(\varphi)$ and the density $\rho(\varphi)$ as functions of the phase variable $\varphi \in [0, 1]$, namely

$$\frac{d\psi}{d\varphi} = \frac{B(\rho,\varphi)}{\psi} - \lambda \tag{18}$$

$$\frac{d\rho}{d\varphi} = -\frac{C(\rho,\varphi)}{A(\rho,\varphi)} + \lambda \frac{\varphi(\rho_2 - \rho)}{d_0 A(\rho,\varphi)\psi}, \tag{19}$$

has a (unique) solution satisfying $\psi(\varphi) > 0$ for $0 < \varphi < 1$ and the following boundary conditions

$$\psi(0) = \psi(1) = 0 \tag{20}$$

$$\rho(0) = \rho_1, \rho(1) = \rho_2 \tag{21}$$

for given density levels ρ_1 and ρ_2. Definitions of the parameter functions in (18) and (19) can be found in [1], Eq. (7.3). When integrating Eqs. (18) and (19), the boundary conditions above impose two compatibility conditions. One is for the free parameter

$$\lambda = \int_0^1 \frac{B(\rho(\varphi), \varphi)}{\psi(\varphi)} d\varphi \,, \tag{22}$$

representing the relative speed of the sharp transition layer. The other is a condition for the ρ-level difference

$$\rho_2 - \rho_1 = \int_0^1 \frac{1}{A(\rho(\varphi), \varphi)} \left[\lambda \frac{\varphi\,(\rho_2 - \rho(\varphi))}{d_0 \psi(\varphi)} - C(\rho(\varphi), \varphi) \right] d\varphi \,. \tag{23}$$

Below we will show that in cases of positive λ, meaning a 'dissolving' boundary of the ordered domain, this condition determines an additional free integration constant c. However, for negative λ, meaning a 'growing' boundary of the ordered domain, it imposes a compatibility relation between ρ_2 and ρ_1.

Since the boundaries of the unit interval are degenerate points of the ODE system (18) and (19), one has to construct the asymptotics for $\rho(\varphi)$ and $\psi(\varphi)$ in the limit $\varphi \to 0$ and 1, for more details see [1], Sect. 7. In particular, ρ has the following expansion near $\varphi = 1$:

$$\rho(\varphi) = \rho_2 - c(1-\varphi)^\kappa - \frac{\gamma}{2-\kappa}(1-\varphi)^2 + O((1-\varphi)^3) \tag{24}$$

with $\kappa \sim \lambda$ and the integration constant c determined by condition (23). However, it follows that for the case $\lambda < 0$, and consequently $\kappa < 0$, the boundary condition $\rho(1) = \rho_2$ can only be satisfied with $c = 0$.

We now solve the given boundary value problem by the following numerical shooting method, which is slightly different from the method applied in [1] and generally more stable. First, using the asymptotic expressions, particularly (24), we determine the values of the functions ψ and ρ near particular points $\varphi = \delta$ and $1 - \delta$, with a positive distance $\delta \ll 1$. Taking these values as initial data for the ODE system (18) and (19), we solve this system numerically from both sides till the point $\varphi = 1/2$. Thus we get two values for each function. For example, for the function $\psi(\varphi)$, we get $\psi(1/2)_-$ and $\psi(1/2)_+$, where subscripts $-$ and $+$ indicate from which side we have started the integration process.

4.1 Case of Dissolving Ordered Monolayer: $\lambda > 0$

We construct the error functions

$$F_1(\lambda, c, \rho_1, \rho_2) = \psi(1/2)_- - \psi(1/2)_+ \tag{25}$$

$$F_2(\lambda, c, \rho_1, \rho_2) = \rho(1/2)_- - \rho(1/2)_+ \tag{26}$$

where c is the constant of integration in (24). For any given pair of levels $\rho_1 > 0$ and $\rho_2 > 0$ both values λ and c are taken as free parameters. Using a standard recurrent iteration method with suitably chosen relaxation constants, the values converge to a unique pair $\{\hat{\lambda}, \hat{c}\}$ satisfying the zero-error condition

$$F_1(\hat{\lambda}, \hat{c}, \rho_1, \rho_2) = F_2(\hat{\lambda}, \hat{c}, \rho_1, \rho_2) = 0\,. \tag{27}$$

Then we have solved the boundary value problem (18)–(21) and found the corresponding wave speed value $\lambda = \hat{\lambda}$, as long as $\hat{\lambda} \geq 0$. If this fails, we have to switch to the next case.

4.2 Case of Growing Ordered Monolayer: $\lambda < 0$

For the case $\lambda < 0$ the parameter c has to be zero and we cannot solve system (27) for any pair of $\{\rho_1, \rho_2\}$, since we have only one free parameter λ for two equations. In this case a solution is possible only for a special curve in the $\{\rho_1, \rho_2\}$ plane, which then satisfies condition (23). Thus, we perform the same iteration procedure in order to reduce the error functions F_i for $c = 0$ and fixed ρ_1 but with varying free parameters (λ, ρ_2). Then, convergence towards values $\hat{\lambda}$ and $\widehat{\rho_2} = \widehat{\rho_2}(\rho_1)$ satisfying

$$F_1(\hat{\lambda}, 0, \rho_1, \widehat{\rho_2}) = F_2(\hat{\lambda}, 0, \rho_1, \widehat{\rho_2}) = 0 \tag{28}$$

yields a solution with $\hat{\lambda} < 0$.

4.3 Simulation Results

With a chosen parameter set (the same as in [1]), extensive numerical computations reveal that only for values $\rho_1 \lesssim 0.45$ and $\rho_1 \gtrsim 7$ we find $\lambda > 0$, but in-between λ is negative. Figure 5 depicts the points in the (ρ_1, ρ_2) plane allowing for a solution of the transition problem (18–21). Two grey areas on the right and on the left are shown, where solutions exist with positive wave speed λ. In-between the curve $\rho_2 = \widehat{\rho_2}(\rho_1)$ is plotted on which λ is negative. At the endpoints of this curve we have two point singularities representing particular states with $\lambda = 0$.

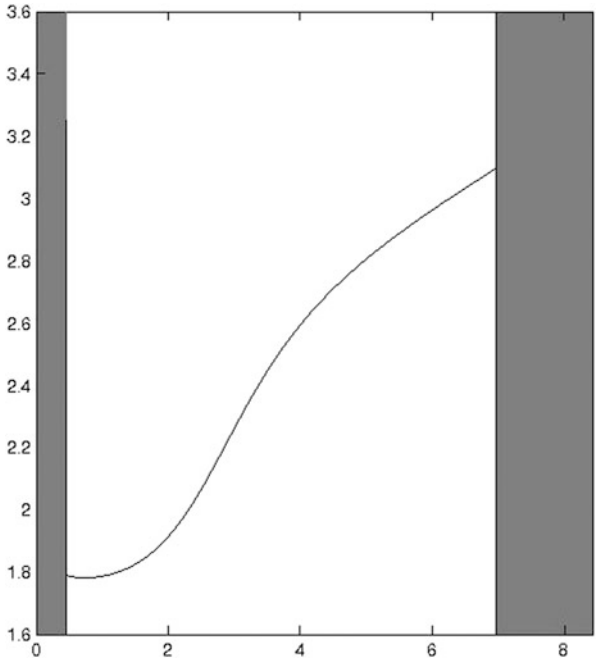

Fig. 5 Diagram of possible lipid phase transitions projected to the (ρ_1, ρ_2) plane of asymptotic boundary values. *Dark grey* areas correspond to positive λ values. In-between the curve $\rho_2 = \widehat{\rho_2}(\rho_1)$ is plotted, on which λ is negative. The two end points of this curve are isolated singularities (ρ_1^*, ρ_2^*)

In [1], Sect. 8, the full two-phase lipid dynamics with sharp phase transition was numerically investigated for the one-dimensional case of a fixed bounded interval [0, X], where no-flux boundary conditions were imposed for the two outer densities $\rho_1(t, x)$, for $x < s(t)$, and $\rho_2(t, x)$, for $x > s(t)$, respectively. Here $x = s(t)$ defines the moving sharp transition interface. If solutions start with an initial sharp transition not too near to the boundaries, they generally converge to the unique steady state with the singular transition levels $\rho_1 = \rho_1^* \approx 0.45$ and $\rho_2 = \rho_2^* = \widehat{\rho_2}(\rho_1^*) \approx 1.79$, representing the singularity in Fig. 5 with lower ρ_1^* value. For initial data to the left of the singularity, with $\rho_1|_{t=0} < \rho_1^*$, both $\lambda(t)$ and $\dot{s}(t)$ become positive, and the (ρ_1, ρ_2) trajectories approach the projected stable manifold of the singular steady state, see [1], Fig. 14. For initial data to the right of the singularity, with $\rho_1|_{t=0} > \rho_1^*$ and $\rho_2|_{t=0} = \widehat{\rho_2}(\rho_1|_{t=0})$, both $\lambda(t)$ and $\dot{s}(t)$ are negative and the (ρ_1, ρ_2) trajectories stay on the singular curve (in Fig. 5), constituting the other side of the projected stable manifold, on which they asymptotically approach the same singular steady state.

However, the so far unsolved question is, what happens with the sharp transition approximation, if the transition levels hit the 'border line', namely $\rho_1(t) = \rho_1^*$, while $\rho_2(t) \neq \rho_2^*$. In Fig. 6a we plot the numerically computed transition profiles of the density function $\rho(\varphi)$ for different boundary values $\rho_1 < \rho_1^*$ and

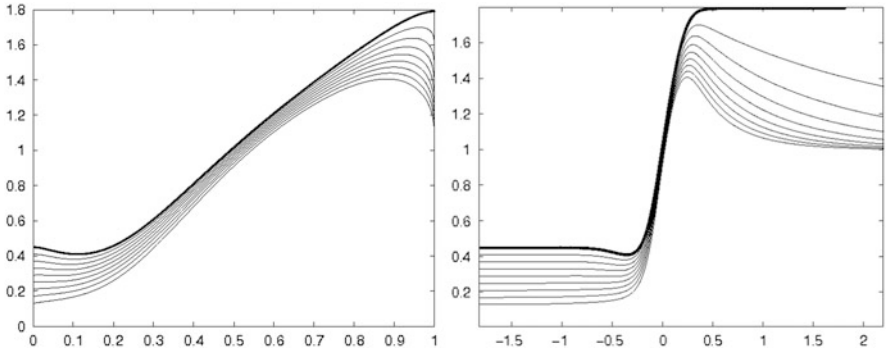

Fig. 6 (**a**) *Left*: Functions $\rho(\varphi)$ for different boundary values $\rho_1 < \rho_1^*$ and for fixed $\rho_2 = 1$. When approaching the critical value $\rho_1 = \rho_1^*$ monotonically from below, the profiles also monotonically increase and approach the thick graph $\rho^*(\varphi)$. Their maximal values $\rho_{max} = \max \rho(\varphi) = \rho(\varphi^*)$ converge to $\rho_2^* > 1$, however, φ^* converges to the right hand boundary $\varphi = 1$. (**b**) *Right*: The profiles $\rho(\xi)$ for different boundary values $\rho(-\infty) = \rho_1 < \rho_1^*$ and for fixed $\rho(\infty) = \rho_2 = 1$. When monotonically approaching the critical value $\rho_1 = \rho_1^*$, the profiles also monotonically increase and approach the thick graph $\rho^*(\xi)$ but with decaying rate of exponential convergence $\rho(\xi) \to \rho_2$ for $\rho_1 \to \rho_1^*$

fixed $\rho_2 = 1 < \rho_2^*$. As we can see, when $\rho_1 \to \rho_1^*$, the profiles $\rho(\varphi)$ approach an asymptotic profile with $\lambda = 0$, namely $\rho^*(\varphi)$, which is plotted as a bold graph. This is the unique singular transition profile connecting ρ_1^* with ρ_2^*, so that the right hand boundary value is strictly larger than the prescribed value $\rho_2 = 1$ of all the other ρ profiles. This means that, the closer we come to the boundary value $\rho_1 = \rho_1^*$, the thinner becomes the boundary layer in the neighborhood of $\varphi \sim 1$.

If we plot the density profiles of the transition layer over the physical space coordinate ξ, we obtain the graphs in Fig. 6b. It is obvious that the decreasing boundary layer near $\varphi = 1$, described in Fig. 6a, corresponds to a decreasing exponential rate of convergence $\rho(\xi) \to 1$ for $\xi \to \infty$. Thus, when approaching the boundary of the left $\{\lambda > 0\}$ region in Fig. 5, the wave speed λ converges to zero, but the convergence towards the singular $\rho^*(\xi)$ profile is non-uniform in space, except when we approach the singularity (ρ_1^*, ρ_2^*). We conclude that the approximate equations (18) and (19) for a thin transition layer loose its validity near the $\{\lambda = 0\}$ borders away from the singular points.

5 One-Dimensional Simulation of the Continuum Phase Field Model

For exploring the quantitative solution behavior around the singular point and for simulating the effects of cyclic breathing, we rely on the original phase field continuum equations (15)–(17) for positive ε with no-flux boundary conditions on a

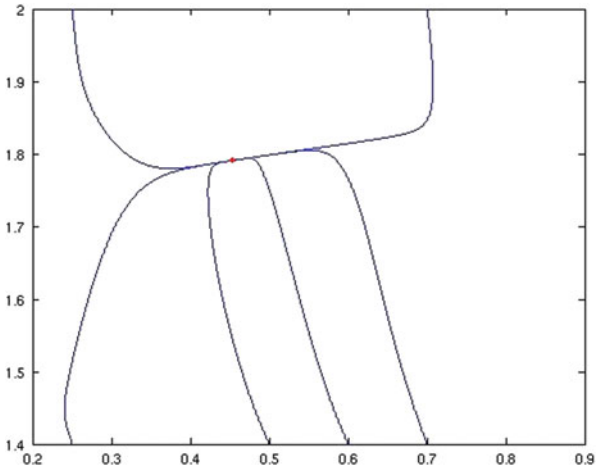

Fig. 7 Trajectories of the (ρ_1, ρ_2) values in simulations of the phase field equations (15)–(17), for six different initial conditions, converging to the asymptotically stable singularity $(\tilde{\rho}_1^*, \tilde{\rho}_2^*)$ (*red dot*)

given interval $[0, X]$. We perform numerical simulations for the qualitatively same situation as in Sect. 4.3, namely a phase separation of the interval into a left hand part with unordered and a right hand part with ordered lipids.

5.1 Smoothed Phase Separation in a Fixed Interval

On the unit interval $\{0 < x < 1\}$ we choose the initial distribution of the phase field φ to be zero in $0 < x < s_0$ and one in $s_0 < x < 1$ for some transition point $0 < s_0 < 1$. Accordingly, for the density ρ we take step distributions with different plateau values $\rho(0) = \rho_1$ and $\rho(1) = \rho_2$. Since the partial differential equations (15)–(17) with positive $\varepsilon(= 0.05)$ constitute a well-posed parabolic-elliptic system with regularity properties, also when discretized by using a standard explicit scheme with finite elements, the initial step data are smoothed instantaneously.

In all simulation runs we observe evolution to the same stationary state $\tilde{\rho}$ with boundary values $\tilde{\rho}_1^* \approx 1.79$ and $\tilde{\rho}_2^* \approx 0.47$, both quite close to the coordinates of the sharp transition singular point (ρ_1^*, ρ_2^*), see the trajectories in Fig. 7. The plots in Fig. 8a show the density profiles of a specific trajectory at different times. One can easily see the convergence towards a stationary profile, which is approximately the same as the asymptotic profile in Fig. 6b. Starting point of the phase transition interface was $s_0 = 0.35$. Depending on the initial data, the position of the interface $s(t)$ moves backward or forward (the latter is to be seen in Fig. 8b) and converges to an asymptotic value (to be seen in Fig. 9a). Simultaneously, the relative speed parameter $\lambda(t)$ converges to zero (see Fig. 9b).

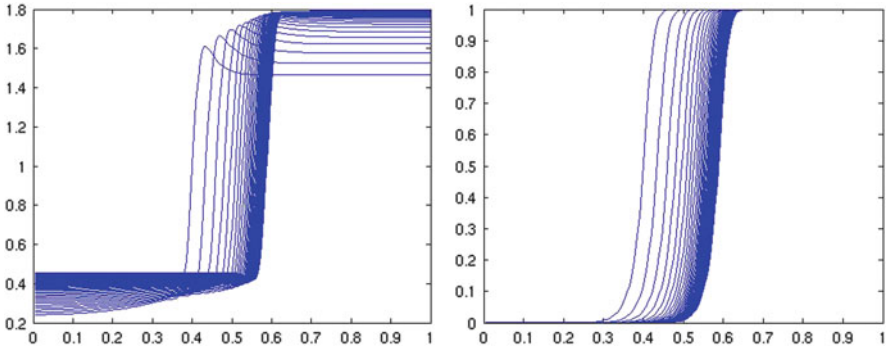

Fig. 8 (**a**) *Left*: time evolution of the density profiles $\rho(t, x)$ for one specific initial condition $(\rho_1, \rho_2) = (0.25, 1.4)$ with $\lambda(t) > 0$. (**b**) *Right*: the corresponding phase transition functions $\varphi(t, x)$

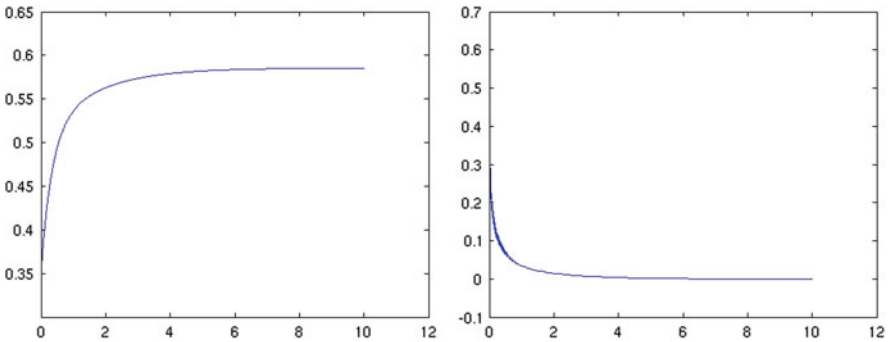

Fig. 9 Simulation as in Fig. 8. (**a**) *Left*: the 'interface' position $s(t)$, where $\varphi(t, s(t)) = 0.5$. (**b**) *Right*: the function $\lambda(t) := \dot{s}(t) - V(t, s(t))$

5.2 *Phase Separation Behavior in an Oscillating Domain Simulating "Breathing"*

In order to mimic the alveoli expansion and compression during breathing, we make our domain $\{0 < x < X(t)\}$ to change periodically its size, for instance in a sinusoidal manner: $X(t) = X_0(1 + a \sin \omega t)$ with $X_0 = 1$ (comparable to μm), breathing amplitude $a = 0.5$ and breathing frequency $\omega = 2\pi$ (comparable to 1.26/s). As can be observed from the density profile plots of Fig. 10a, it is the 'exhalation' period during which the interval size $X(t)$ shrinks and thereby both densities of disordered and ordered lipids are lifted up while, after a certain time lag, the transition interface starts to move left and leads to a quite fast growth of the ordered lipid monolayer. Then the reverse process can be observed during the

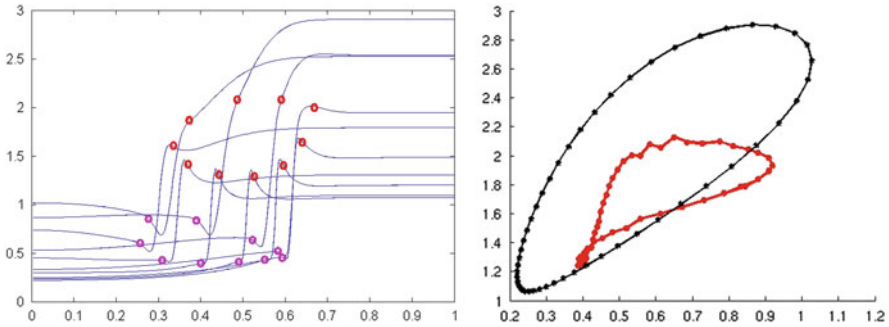

Fig. 10 'Breathing' cycle simulation of the phase field model with $\varepsilon = 0.05$. (**a**) *Left*: time evolution of the profile $\rho(t, \tilde{x})$ over the rescaled variable $\tilde{x} = x/X(t)$ on the fixed unit interval. The $\tilde{\rho}_2(t)$-values just right of the transition layer together with their position values $\tilde{x}_2(t)$ describe a counter-clockwise cycle (*red circles*). A similar but smaller cycle is described by the $\tilde{\rho}_1(t)$-values just left of the transition layer together with their position values $\tilde{x}_1(t)$ (*magenta circles*). (**b**) *Right*: corresponding clockwise trajectories of the level pairs (ρ_1, ρ_2) at the interval boundaries (*black curve*) and $(\tilde{\rho}_1, \tilde{\rho}_2)$ near the transition layer (*red curve*). Notice that the simultaneous decrease of both values during 'inhalation' is much faster than the increase during 'exhalation'

'inhalation' period, when due to the growth of interval size $X(t)$ both ρ_1- and ρ_2-levels rapidly decrease while, again after a time lag, the transition interface moves to the right and the ordered lipid monolayer shrinks.

Due to strong diffusion in the disordered phase, inducing long slopes in the density profile, the left boundary values $\rho_1(t)$ oscillate much stronger than the $\tilde{\rho}_1(t)$-values directly left of the transition zone; the same is true for the corresponding $\rho_2(t)$- and $\tilde{\rho}_2(t)$-levels of the ordered phase to the right, compare the 'circle dots' in Fig. 10a and the corresponding trajectories plotted in Fig. 10b. The inner hysteresis loop (red curve) is not only smaller but also strongly deformed compared to the outer, more ellipsoid hysteresis loop (black curve). This is mainly due to the strong difference $\rho_2(t) - \tilde{\rho}_2(t)$ during the 'exhalation' period, when ρ_2 still increases, while $\tilde{\rho}_2$ already begins to decrease and the transition front moves to the left so rapidly, that there appears a larger secondary transition zone (of size up to 0.25) between the sharp transition layer and the ρ_2-plateau. Simultaneously, also the relative speed $\lambda(t)$ becomes negative, so that the $(\tilde{\rho}_1, \tilde{\rho}_2)$-trajectory enters the 'forbidden region' of Fig. 5, consistent with the result of Sect. 4, that in this region the fast transition approximation breaks down.

Finally, we have simulated more realistic breathing cycles with shorter inhalation and longer exhalation period, where in both cases the expanding or compressing interval length $X(t)$ exponentially tends to a potential steady state: The cycle duration is 0.5 time units (comparable to 5 s) with 0.2 for inhalation and 0.3 for exhalation (see Fig. 11a). This time we used a doubled transition parameter $\varepsilon = 0.1$, resulting in a broader transition layer for the density profiles (see Fig. 12a). Again, as in Fig. 10b, the trajectories in the (ρ_1, ρ_2) state space (Fig. 12b) show a clear hysteresis behavior. Now the inner cycle of $\tilde{\rho}$ levels near the transition zone is

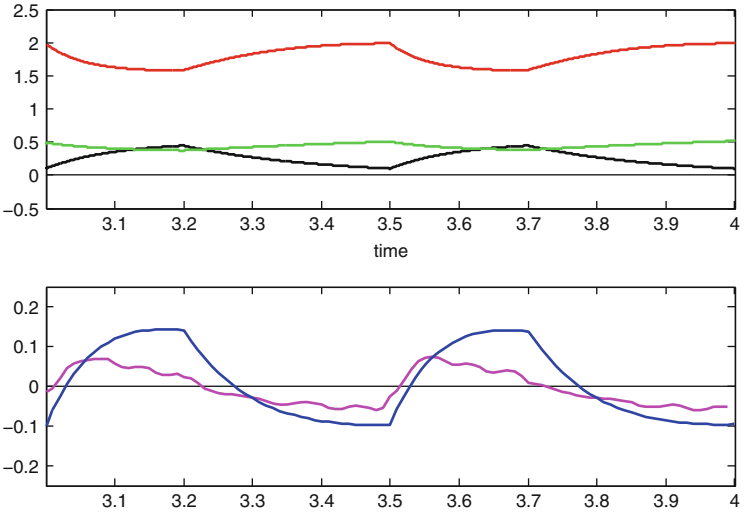

Fig. 11 Two cycles of a more realistic 'breathing' simulation with $\varepsilon = 0.1$. (**a**) *Upper plots*: the interval excess length $X(t) - 1$ (*black*) shows exponential curves with shorter 'inhalation' and longer 'exhalation'; also plotted are the resulting boundary values $\rho_1(t)$ and $\rho_2(t)$ (*green* and *red graphs*, respectively). (**b**) *Lower plots*: the resulting viscous transport velocity $V(t, s(t))$ at the middle point $s(t)$ of the smooth transition (*blue graph*) and the corresponding relative speed parameter $\lambda(t) = \dot{s}(t) - V(t, s(t))$ (*magenta graph*)

not so much reduced in size, but only shifted to higher ρ_1 values in such a way that the transition singularity (compare the small dot in Fig. 7) lies in the center of this hysteresis loop. This again is consistent with the results in Sect. 4, since the upper part of the hysteresis trajectory, roughly above this singularity, shows values $\lambda(t) < 0$, see Fig. 12b, what can also be checked by the time plot in Fig. 11b.

It is worthwhile to have a closer look at the $(\tilde{x}_2, \tilde{\rho}_2)$ cycle in the upper part of Fig. 12a: During 'in- or exhalation' there is first a period of changing $\tilde{\rho}_2$ levels with relatively constant $\tilde{x}_2$, meaning also a constant phase transition zone, followed by a period with changing position of the transition zone, while the $\tilde{\rho}_2$ level stays constant. Obviously this is a characteristic dynamic feature of the ordered monolayer. During a fast change of the interval size, the following two subsequent events take place: first, the lipid density is passively adjusted to the changing pressure, then, as a reactive process at the phase boundary of the monolayer, disordered lipids are associated or dissociated, respectively, while simultaneously the pressure adapts due to viscous flow within the monolayer.

Summarizing the simulation results of this section we can state that both 'breathing cycle' models are able to reproduce the hysteresis property, which has been experimentally observed from plotting the density-pressure isotherm curves (see Fig. 1). Such a curve can be expected also in our simulation, since the total pressure in Eq. (13) explicitly depends on the ρ and φ profiles.

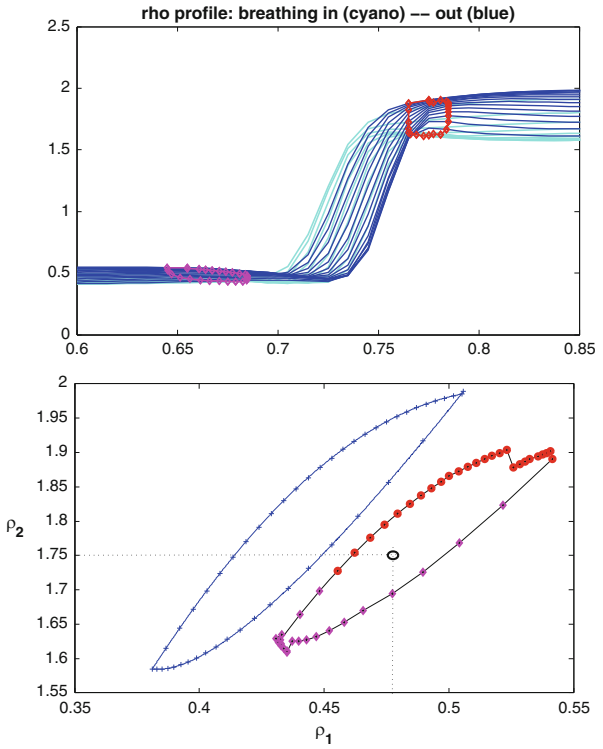

Fig. 12 Simulation of one periodic 'breathing' cycle as in Fig. 11: (**a**) *Top*: zoomed plots of density profiles $\rho(\tilde{x})$ with depicted points $(\tilde{x}_1, \tilde{\rho}_1)$ and $(\tilde{x}_2, \tilde{\rho}_2)$ left and right of the phase transition zone (*magenta* and *red dots*, respectively), cycling in a counter-clockwise sense. (**b**) *Bottom*: corresponding clockwise trajectories of boundary values (ρ_1, ρ_2) (*blue curve*) and of $(\tilde{\rho}_1, \tilde{\rho}_2)$ (*magenta diamonds* when $\lambda > 0$, and *red circles* when $\lambda < 0$), the latter cycling around the approximate steady-state singularity $(\tilde{\rho}_1^*, \tilde{\rho}_2^*)$ (*small ellipse*)

6 Conclusions

In extension of the results in [1] we demonstrated, how the mesoscopic continuum phase transition model can produce realistic simulations of a periodically expanded and compressed one-dimensional water surface with an embedded lipid monolayer on top. The observed phenomenon of hysteresis could be reproduced and further dynamical properties of the 'patchy' lipid monolayer system were revealed, which characterize its suspected functional role as an adaptive surfactant buffering system during breathing of the lung.

Moreover, a simple model for the stochastic motion and interaction of amphiphilic lipids as stiff rods on top of a fixed water surface was introduced and numerically simulated. The essential dynamics of ordered monolayer clustering from a reservoir of disordered diffusing lipids were realized under varying parameter

conditions. In spite of its simplicity, this microscopic submodel could serve as an effective tool to study further connections between the detailed molecular interaction parameters and the lumped reaction parameters in the continuum two-phase mixture model.

Acknowledgements The presented results have been elaborated within the research program of the SFB 611 in Project B7. For the effective cooperation during 12 years we express cordial thanks to the co-leader, Hans Wilhelm Alt, moreover, to all coworkers and former members of our project and, in particular, to Martin Rumpf and his coworkers in Project B8. We also thank our former colleague Steven Perry from the Zoological Institute in Bonn for offering the lung alveoli surfactant problem in the starting phase of the project and for mediating the physiological literature.

References

1. Alt, H.W., Alt, W.: Phase boundary dynamics: transition between ordered and disordered lipid monolayers. Interfaces Free Bound. **11**, 1–36 (2009)
2. Alt, H.W., Alt, W.: Fluid mixtures and applications to biological systems. This volume, pp. 191–219 (2013)
3. Ding, J., Takamoto, D.Y., von Nahmen, A., Lipp, M.M., Lee, K.Y.C., Waring, A.J., Zasadzinski, J.A.: Effects of lung surfactant proteins, SP-B and SP-C, and palmitic acid on monolayer stability. Biophys. J. **80**, 2262–2272 (2001)
4. Knecht, V., Bonn, M., Marrink, S.-J., Mark, A.E.: Simulation studies of pore and domain formation in a phospholipid monolayer. J. Chem. Phys. **122**, 024704 (2005)
5. Nemadjieu, S.F.: Finite volume methods for advection diffusion on moving interfaces and application on surfactant driven thin film flow. Dissertation, University of Bonn (2012)